Supplementary Materials

Materials and Methods

Photosystem II Preparation:

PSII-enriched thylakoid-membrane particles were prepared from supermarket spinach [1,2]. Prior to use, samples were stored at -80°C in a buffer using sucrose as a cryo-protectant: 0.4 M sucrose, 5 mM $CaCl_2$, 5 mM $MgCl_2$, and 15 mM NaCl, 50 mM MES, pH 6.0. The oxygen evolution activity of PSII was measured by a Clark-type electrode in a Hansatech oxygraph. The activity of the preparation was 300 µmol O_2/(mg Chl • hr) or greater under constant saturating illumination at 25°C utilizing 0.3 mM 2,6-dichloro-1,4-benzoquinone (DCBQ) as an artificial electron acceptor. The Chl a:b ratio was derived from the optical absorbance of chlorophyll extracted with 80% acetone: 20% water solution. This was measured with a Cary300 Bio UV-visible spectrophotometer. For all samples, this ratio was ~2.5:1 which indicates high enrichment of membrane particles with PSII. To ensure the high quality of the samples, low temperature X-band EPR spectra were recorded for the S_1 and S_2 states. S_2 state samples were obtained by illuminating S_1 state samples with 120 W Halogen lamp for 30 minutes while in a cold bath of ethanol and dry ice to maintain a sample temperature of 195 K, after which they were immediately frozen in liquid nitrogen.

For TR-XES, the PSII samples were prepared on-site immediately prior to the measurements as follows. After thawing the stock pellet (~30mg Chl/mL) stored on dry ice for travel, the samples were diluted 1:1 with a 30% v/v glycerol in a buffer of 5 mM $CaCl_2$, 5 mM $MgCl_2$, and 15 mM NaCl, 50 mM MES, pH 6.5 and homogenized gently with a paintbrush. A solution of 50 mM PPBQ in DMSO was added to yield a final PPBQ concentration of 500 µM [3,4]. The sample was painted onto clean mixed fiber thread (Coats & Clark Cotton Machine Quilting Thread) of radius ~175 µm with a soft brush. Painting ensures the best sample absorption onto the threads. Possible Mn contamination of the threads was tested by subjecting them to 1) a 10 minute exposure to X-rays under the exact conditions of PSII data collection (i.e. a clean thread was pulled through our collection system with fluorescence recorded by the spectrometer) and 2) a ~20 minute exposure to a much brighter X-ray source, during which fluorescence was recorded by an energy-resolving detector. Threads were found to contain no detectable Mn contamination and remained intact following both X-ray and laser exposure. Threads were wound onto small plastic spools and servo motors were used to slowly wind and unwind the threads between the plastic spools at a constant speed during painting. During measurements, the spool with freshly painted thread was placed on an axis above a reservoir of ice and covered with aluminum foil. Measurements were performed as soon as possible (<30 min from application of sample to data collection) and the sample was maintained at 4 ℃ until directly before measurement. All sample preparation, handling and storage environments were completely dark, save for dim green LEDs when unavoidable, to prevent state transitions prior to measurement. In addition, samples were maintained at a constant temperature of approximately 4 °C during preparation.

Beamline Description:

TR emission spectra were collected at beamline 14-ID B, BioCARS [5], of the Advanced Photon Source, Argonne National Lab with an electron energy of 7.0 GeV and an average current of 100 mA. To avoid second order reflections and gallium fluorescence inherent to the spectrometer crystals, the undulator gap of U27 was set to 11.7 mm during the emission

experiments yielding a ~500 eV FWHM undulator spectrum centered around 7.85 keV. In addition, the water-cooled KB mirrors for focusing were translated to their Si stripes and set to an angle of 3.8 mrad, thereby cutting the incident energy range sharply above the energy of the first harmonic. The vertical mirror was defocused to yield a final projection size of ~45 x 100 μm^2 (V x H) given the sample surface angled 45° to the incident beam, and the incident flux was monitored downstream of both mirrors via a photodiode. X-ray pulses of ~44 μs were produced using the high heat load chopper [5] and delivered at frequency 10.3 or 20.6 Hz, see Table S1 for experimental parameters. The number of x-ray bunches (dark purple) per 44 μs pulse is variable, depending on storage ring parameters during each beamtime. Data sets 1-3 had approximately 4000, data sets 4 & 5 only ~300. Note that the overall x-ray dose was the same.

Monochromatic beam was produced using a Si(111) channel-cut monochromator inserted into the beam path and calibrated via the $KMnO_4$ pre-edge at 6.5433 keV. Monochromatized beam is necessary for the energy calibration of the position sensitive detector. The smallest possible undulator gap (10.5 mm), corresponding to a peak energy of 6.85 keV, was used such that the tails of the undulator spectrum reach 6.445 keV, the lowest collection energy of the GaP spectrometer. To improve the energy resolution of x-rays reflected by the monochromator, the beam incident on the channel-cut was collimated by decreasing the radius of curvature of the vertical mirror. The scattering signal used for calibration was collected with 1 kHz pulse frequency to increase the integrated flux.

XES Spectrometer:

For this study, we utilized a short working distance (SWD) miniature x-ray emission spectrometer (miniXES) in which multiple flat dispersive GaP 110 analyzers reflect x-ray fluorescence onto a Pilatus 100k (Dectris) 2-dimensional position sensitive detector (2D-PSD) Figures 1D & S1B [6,7]. To decrease attenuation, the internal spectrometer space is purged with He during use. The spectrometer crystals are arranged in a von Hamos geometry and designed for a collection range of ~50 eV about the Kβ main lines, with each crystal reflecting the complete Mn Kβ spectrum (6445-6510 eV) onto the PSD, Figures 1D & S1B. The width of monochromatic elastic scatter measured by the spectrometer is a convolution of the monochromator spectral resolution ($\Delta E/E = 1.4 \times 10^{-4}$) and the broadening introduced by the spectrometer itself, determined to be ~0.3 eV. Note that this resolution is distinct from the minimum energy shifts resolvable by the setup; our maximum obtained resolution is discussed in **Data Processing / Averaging**.

Prior to measurements, the spectrometer was aligned horizontally and vertically via eyelets designed for this purpose. The thread position with respect to the spectrometer in the beam direction (see more in **Sample Positioning**) was optimized prior to PS II data collection using a sample with intense Mn Kβ fluorescent signal, typically $MnCl_2$ solution painted on the threads. Multiple small (~100 μm) sample translations along the beam direction were implemented until all 10 crystals were fully visible on the Pilatus face. The thread position in the beam direction was fixed using the focus of a stationary, high magnification camera. A lens extension with a focal depth of ~50 μm was used to ensure consistent spatial positioning.

Sample Positioning:

To provide the least amount of stray scatter into the spectrometer aperture, the samples were tilted vertically 45° towards the incident beam, Figure S1C. Kinematic mounts were used to attach the sample delivery system, Figure S1C, to a motorized X,Y,Z stage. These mounts provide a simple, highly reproducible method for exchanging samples with minimal shifts of thread

position relative to the spectrometer. Immediately following the sample mounting procedure, the thread was aligned with the x-ray beam via a computerized transmission scan perpendicular to the beam (inboard/outboard – $\hat{x}$ in Figure S1B) using the downstream diode (Thorlabs PDA36A). To prevent the destruction of the diode, a reduction in beam intensity was necessary in addition to a protective layer of attenuation foil on the diode. Once the center of the thread was confirmed horizontally, the thread was brought into the focal point of the camera using the vertical and along-the-beam motors ($\hat{y}$ and $\hat{z}$ respectively, in Figure S1B), with the inboard/outboard ($\hat{x}$) position held constant. Typically, a few small steps of 50-100 μm were required.

The sample delivery system, Figure S1C, includes plastic goal posts protruding from an aluminum plate and angled 45° to the beam. Stainless steel syringe needles of radius 203 μm are securely fitted through holes in these posts to deliver sample reproducibly at the beam position. The needles are positioned far outside of the spectrometer's acceptance volume to prevent contamination from ancillary Mn. A stepper motor is mounted on the upstream side of the sample assembly, and an aluminum spool of starting radius 9.55 mm or 11.2 mm (data set #1 only, see Table S1 for an experimental summary) is attached to the motor to pull and collect thread as it passes through the interaction region. See Figure S1C. In general, sample positions were not changed except upon mounting and aligning in small increments as determined by transmission scan and by the camera system, see more in **Establishing the Interaction Region and Timing Schemes**. Note that the sample coated spool was covered completely with aluminum foil during the positioning time to prevent any unintentional x-ray or light exposure that could alter the protein state prematurely. Once the sample position was finalized, this covering was partially removed to allow free translation of the thread, and the collection spool was rotated repeatedly until the previously enclosed fresh sample reached the beam position.

Spectrometer Calibration:

An *in situ* calibration of the detector pixels is achieved by measuring the positions of the elastic scattering peaks while scanning the monochromator through the x-ray emission energy range (6445-6510 eV). The calibration methodology has been described in detail elsewhere [8-10]. Note that the line width of the elastic peaks is the convolution of the monochromator and spectrometer energy resolutions. It is important to recognize that changes in sample position relative to the spectrometer alter the detector calibration. We thus developed a system to reproducibly position the sample (tolerance <50 μm), and calibrated the spectrometer daily following the completion of measurements on a given sample (typical sample consisted of 6-8 m of painted thread). In addition to this, $MnCl_2$ solution emission spectra were collected after each sample on the same thread without any sample repositioning. These spectra were used as an internal reference.

Establishing the Interaction Region and Timing Schemes:

Pump/probe Alignment and Camera Setup:

In addition to the criticality of reproducible sample position in the miniXES system, exact alignment between laser and x-ray is crucial for accurate TR data. Light excitation was provided by a Spectra-Physics Empower laser (527 nm, pulse length ~200 ns) placed at an angle θ~5° to the incident x-ray beam. Additional optics allowed for a FWHM spot size of ~220 μm, at a laser fluence of ~11 mJ/mm^2. The laser spot size was selected to be about twice larger than x-ray spot

size to ensure best alignment. The x-ray beam was visualized on a phosphor (SPI P47 coated scintillator) positioned at the previously established sample position relative to the spectrometer and the laser was moved to an overlapping position.

To facilitate fine adjustments to the sample alignment and monitor the interaction region during data collection, a Prosilica camera directed at the sample was mounted vertically on a small X,Y,Z stage. To improve our precision, a lens extension with a focal depth of ~50 μm was used. Once in place, the focal region of the camera was aligned to a test thread known to be in alignment with the spectrometer setup. The thread was then removed and replaced by the phosphor mounted at the same position, see Figure S1C. It is critical that the phosphor surface appears in focus on the camera. x-ray/laser alignment was checked periodically using the phosphor. No deviations were found during 4 days of beamtime. Once these alignments are complete, fine adjustments of the sample/spectrometer alignment for optimal emission signal are made by small spectrometer translations only. From that point the sample position is 'fixed' at the focal region of the camera, the spectrometer position is finalized, and data collection starts.

X-ray/Laser Synchronization:

For verification of timing, the phosphor was replaced by a small Si photodiode aligned at the beam position (in the focus of the camera). Synchronization between the pump (laser) and probe (x-ray) pulses was performed by recording the respective diode signals on an oscilloscope. A field programmable gate array (FPGA) was used to maintain the timing between the laser and x-ray pulses. The programmable delay between laser and x-rays pulses was adjusted to overlap in time the peaks of each pulse that was subsequently defined as time zero. Given the broad 44 μs FWHM x-ray and ~200 ns FWHM laser pulses, it is more exact to synchronize via peak position instead of rising edges. It follows that spectra recorded at a set delay include fluorescence from ±20 μs, see Figure S1A.

Photosystem II advancement in the Kok cycle:

In this work, we do not deconvolute the XES spectra but instead analyze changes in the first moments as a function of the number of laser flashes and time delay to the probe pulse. For a prediction of S-state composition, we refer to Han et al. who recently established the maximal experimentally achievable S-state composition after each laser flash at room temperature for PS II membrane preparations from spinach [4]. To ensure the most efficient S-state conversion, we emulate previous experimental laser settings. At a laser fluence of ~11 mJ/mm^2, assuming the threads are fully saturated with sample, the ratio of incident photons to PS II centers lies between ~560 (conservatively, 35 Chl:reaction center) and ~3400, assuming a typical ratio of 200 Chl per reaction center common for PS II-enriched thylakoid membrane fragments. These values are in line with the XES experiment by Messinger et al., in which S-state advancement was determined by EPR [11]. While Messinger et al. manually froze their samples to trap early S-state intermediates, we probe the created S-states long before any decay can occur. As such, we set their published S-state composition values as our expected lower bounds. We therefore expect at least ~65% advancement for each of the 3F time delays, given they are pumped with the same number of laser flashes. As a result of this convolution of states, the magnitude of reductive effects from S_3 to any of the S_4 states will be larger than we observe. It should also be emphasized that convolution with $S_{2,3}$ data is not likely to lessen any oxidative effect more than ~30%.

Data Collection:

Data collection scans were synchronized in the following manner – for parameters α, β and γ see Table S1: (i) the stepper motor translates the sample α microns through the beam position transporting fresh material into the beam; (ii) the specified number of laser flashes are delivered to the fresh sample; (iii) subsequently, the ~44 μs x-ray pulse arrives at a delay, β; (iv) immediately following the closure of the shutter, the cycle repeats. Note that both laser and x-ray pulse at the same frequency γ. During the repetition time, the Pilatus continuously collects a single image. Sample threads were mounted in ~5 to ~10 m lengths and monitored every ~0.5 m resulting in multiple Pilatus images per generated state. These images were directly summed during data processing for improved statistics.

Data processing / averaging

Averaging and a Systematic Error Estimation

To evaluate the effects of adding up data obtained on different (and thus re-positioned relative to spectrometer) threads, we first analyzed the strong $MnCl_2$ spectra. Highly concentrated $MnCl_2$ solution (~1 M) was painted onto each thread at the conclusion of PS II measurements prior to sample exchange, and a single PSD image was collected. First moments were calculated around the range 6490-6495 eV (as the $MnCl_2$ peak is higher in energy than PS II) and a standard deviation of 0.02 eV was found. To verify that summing threads would not affect the resolution, we also checked with data that had been split randomly into two groups and observed shifts between 0.005 – 0.02 eV. Consistent with both these methods, we consider 0.02 eV to be our maximal resolution for PS II XES collection. Note also that averaging of multiple threads broadens the data slightly due to minor variations in thread position. These variations are random and therefore can be assumed to be even about the $K\beta_{1,3}$ peak with limited effect on the first moments. Given the sensitivity to sample positioning, each thread was used to collect all S-states/intermediates and only one calibration file was used to process the data reducing the error due to the calibration files themselves. However, calibrations were still taken daily to ensure large shifts in the monochromator calibration or other major effects did not occur. To completely reduce any effects of position or monochromator calibration drift on our S-state shifts, we collected all spectra in approximately equally intensities (equal number of detector exposures) for every thread. It follows that any changes in the absolute position of the sample do not affect the relative shifts between the states.

Processing PS II spectra

A total of seven beamtimes were accomplished, with two devoted to methodology development and five to data collection. For every beamtime (data sets 1 – 5, Table S1), each TR XES spectrum is a direct summation of the Pilatus exposures for all individual threads using a single calibration. Differing data sets are also summed for greater statistics. Results from different beamtimes were merged using the strong $MnCl_2$ signal as an internal energy-calibration reference. Similar to PS II, all $MnCl_2$ spectra in the data set are summed and calibrated with one calibration file. Note that the fifth data collection beamtime occurred following upgrades to the BioCARS beamline optics that considerably increased background and pose a challenge in merging this dataset with others. For that reason, this beamtime is presented separately and, despite these background artifacts, we observe the same trends as we do in other beamtimes when considering this beamtime alone (Figure S4).

Statistical first moments were analyzed for PS II data processed in different ways: completely unprocessed and after smoothing and background removal, Figures 2 & 3. No significant differences were found in the first moment trends between these methods; errors introduced by processing do not alter unprocessed data trends that are significant to within a 95% confidence interval, see Table 3, Figures 2 & 3.

Examples of data for the S_3 to S_0 transition are shown in Figure S2A. Due to high levels of background, and relatively low statistics, consistent background removal was necessary to reliably compute first moment values for comparison with other published works both past and future. A quartic polynomial was fit to the spectral region excluding the Kβ peaks, Figure S2B. The computed polynomial was then subtracted from the spectrum. Note that removal of a linear background was found to create significant variability in the first moments and is thus insufficient. Data were then normalized to the $K\beta_{1,3}$ peak maximum for the purpose of comparison. For both raw and background subtracted data some variability in the first moment trends between beamtimes persists due to noise in the spectral range. To combat this problem, smoothing techniques were tested.

Wavelet Transforms

The wavelet transform method was chosen to smooth non-physical rapid fluctuations in the data while maintaining the integrity of the spectral shape.
The wavelet transformation of our spectrum f(E) is [12]:

$$w(a, E) = C_{\psi}^{-1/2} a^{-1/2} \int_{-\infty}^{\infty} \psi^* \left(\frac{E' - E}{a} \right) f(E') dE' \qquad (1)$$

where C_{ψ} is a normalization constant. The base wavelet function, $\psi_{a,b}(E) = \psi \left(\frac{E - b}{a} \right)$, is dilated and translated to allow for decomposition of the spectrum. Dilation is described by a ; b characterizes translation. For our purposes, we use the Mexican Hat wavelet function, see equation 2 [12].

$$\psi(E) = (1 - E^2) e^{-E^2/2} \qquad (2)$$

Wavelet functions are calculated for the range of a 0.01 to 30, over the interval 6453.7 eV to 6513 eV. The energy-frequency plane of $w(a,E)$ allows for visualization of the most appropriate cutoff for the dilation parameter a used in the spectral reconstruction. Figure S2C provides an example spectrogram. Note that the intensity in z is determined by the $w(a, E)$ value [12].

Our chosen parameters leave the $K\beta_{1,3}$ peak adequately smoothed but without significant broadening while the Kβ' peak maintains some noisy character. It is possible to completely eradicate noise in Kβ' peak, but the process results in significant broadening and symmetrizing of the $K\beta_{1,3}$ peak, an effect we want to avoid as it can skew the first moment calculations. Figure S2B compares the wavelet reconstruction of $3F_{500\mu s}$ state data to the 'raw' spectrum.

Error Determination:

For some experiments, it is common to present the standard error of the mean (SEM) from the second moment, essentially an evaluation of the error on the first moment (our measure of spectral position, mathematically the weighted arithmetic mean). The SEM can be written as follows:

$$\text{SEM} = \sqrt{\frac{\mu_2}{N}} \text{ and } \mu_2 = \frac{\Sigma_i (E_i - \bar{E})^2 I_i}{\Sigma_i I_i} \tag{3}$$

μ_2 is the weighted second moment calculated from the intensities, I_i, and emission energies, E_i, at every point, as well as the weighted first moment, $\bar{E}$. N is the number of observations. Given that the SEM is highly dependent on the sampling/binning of data into N groups, we prefer to avoid this error analysis method. Additionally, SEM results can be misleading in that overlapping error bars do not necessarily exclude statistically significant differences.

Analysis of Variance

ANalysis **O**f **VA**riance (ANOVA) between experimental groups was used to determine the confidence level for the observed first moment shifts between states. One-way ANOVA, calculated from the first moments of raw unprocessed normalized data, yields the p-values in Figures 2, 3, S4 and Table 3. These values represent the probability of falsely rejecting the null hypothesis, i.e. that a difference in the first moment between the two states listed is a random statistical variation. In this study, we take the 95% confidence interval to be significant.

Analysis of Variance is a collection of statistical models that allows comparison between different statistical groups' means. At its core, ANOVA is compares the mean square error between groups to the mean square error within groups. In using ANOVA, we assume that 1) measurements are normally distributed about the mean, 2) the variances within each group are equal, and 3) measurements are independent. To compute the F statistic (reported in Table 3) of N observations from K groups, we simply take the ratio:

$$F = \frac{MS_{between}}{MS_{within}}$$

With

$$MS_{between} = \frac{\Sigma_i n_i (\bar{Y_i} - \bar{Y})^2}{K - 1}$$

and

$$MS_{within} = \frac{\Sigma_i \Sigma_j (\bar{Y_{ij}} - \bar{Y_j})^2}{N - K}$$

Here, the index i runs over the groups, j runs over observations within a group and Y_{ij} is the ith measurement in the jth group. To obtain a p value from the F value, we compare it to the F-distribution:

$$f(x; d_1, d_2) = \frac{\sqrt{\frac{(d_1 x)^{d_1} (d_2)^{d_2}}{(d_1 x + d_2)^{d_1 + d_2}}}}{x \, \text{B}(\frac{d_1}{2}, \frac{d_2}{2})}$$

With B being the beta function and d_1, d_2 being the degrees of freedom. The p value is determined by:

$$p = \int_F^\infty f(x; d_1, d_2) \, dx$$

7

In other words, p is the probability of obtaining an F score of value F or higher by statistical anomaly. Here we consider $p < 0.05$ (meaning less than a 5% chance of randomly observing such a high F value) to be statistically significant.

The first moment trends for raw data match well with those for smoothed, background-subtracted spectra (i.e. 'processed') within our confidence levels, Figures 2 & 3, Table 3. In other words, for those states in which we reject the null hypothesis, smoothing and background subtraction do not alter the trends in the changes to the first moments. However, ANOVA analysis between the same states (excluding 2F) from different beamtimes shows no statistical variation, $p \geq 0.19$, Tables 3. The only outlier 2F spectrum from data set 3 has a dip on the low energy side of the $K\beta_{1,3}$ peak between 6.485 – 6.488 keV. This noise causes a significant variation in first moments between data sets and skews the mean of summed data to lower energies. Unfortunately, this spectral noise is not easy to remove without completely excluding the 2F data from that beamtime, after which statistical invariance is re-established. To preserve statistics, we include these data.

References

[1]   A. W. Rutherford, *Orientation of Electron-Paramagnetic-Res Signals Arising from Components in Photosystem-II Membranes*, Biochim. Biophys. Acta **807** (1985).

[2]   D. A. Berthold, G. T. Babcock, and C. F. Yocum, *A Highly Resolved, Oxygen-Evolving Photosystem II Preparation from Spinach Thylakoid Membranes. Epr and Electron-Transport Properties*, FEBS Lett. **134** (1981).

[3]   Y. Pushkar, J. Yano, K. Sauer, A. Boussac, and V. K. Yachandra, *Structural Changes in the Mn4Ca Cluster and the Mechanism of Photosynthetic Water Splitting*, P. Natl. Acad. Sci. USA **105** (2008).

[4]   G. Y. Han, F. Mamedov, and S. Styring, *Misses During Water Oxidation in Photosystem II Are S State-Dependent*, J. Biol. Chem. **287** (2012).

[5]   T. Graber *et al.*, *Biocars: A Synchrotron Resource for Time-Resolved X-Ray Science*, J. Synchrotron Radiat. **18** (2011).

[6]   K. M. Davis, I. Kosheleva, R. W. Henning, G. T. Seidler, and Y. Pushkar, *Kinetic Modeling of the X-Ray-Induced Damage to a Metalloprotein*, J. Phys. Chem. B **117** (2013).

[7]   K. M. Davis *et al.*, *Fast Detection Allowing Analysis of Metalloprotein Electronic Structure by X-Ray Emission Spectroscopy at Room Temperature*, J. Phys. Chem. Lett. **3**, 1858 (2012).

[8]   J. I. Pacold *et al.*, *A Miniature X-Ray Emission Spectrometer (miniXES) for High-Pressure Studies in a Diamond Anvil Cell*, J. Synchrotron Radiat. **19** (2012).

[9]   B. A. Mattern, G. T. Seidler, M. Haave, J. I. Pacold, R. A. Gordon, J. Planillo, J. Quintana, and B. Rusthoven, *A Plastic Miniature X-Ray Emission Spectrometer (miniXES) Based on the Cylindrical Von Hamos Geometry*, Rev. Sci. Instrum. **83** (2012).

[10]   B. Dickinson, G. T. Seidler, Z. W. Webb, J. A. Bradley, K. P. Nagle, S. M. Heald, R. A. Gordon, and I. M. Chou, *A Short Working Distance Multiple Crystal X-Ray Spectrometer*, Rev. Sci. Instrum. **79** (2008).

[11]   J. Messinger *et al.*, *Absence of Mn-Centered Oxidation in the S_2 to S_3 Transition:Implications for the Mechanism of Photosynthetic Water Oxidation*, J. Am. Chem. Soc. **123**, 7804 (2001).

[12]   V. K. Henner, P. G. Frick, T. S. Belozerova, and V. G. Solovyev, *Application of Wavelet Analysis to the Spectrum of Omega ' States and Ratio Re+E*, European Physical Journal C **26** (2002).
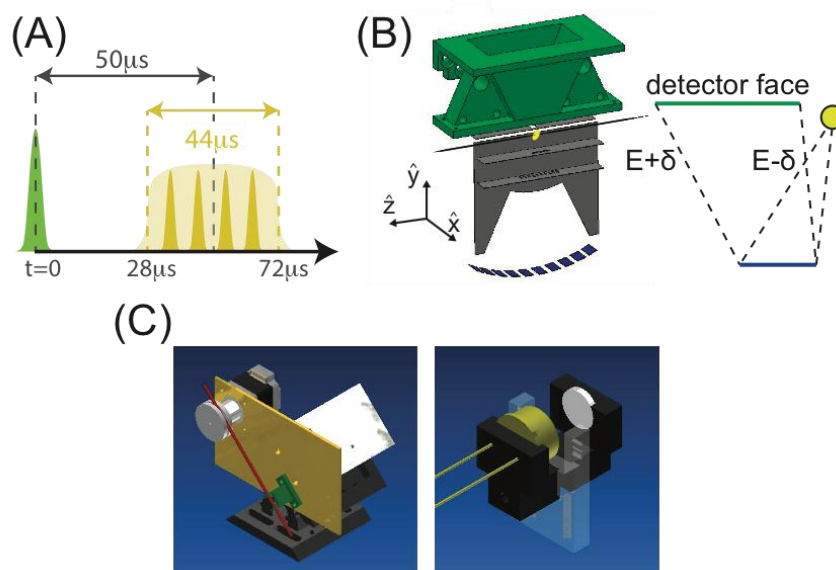
Figure S1. **Details of the TR-XES experimental setup.** (**A**) Sample timing scheme depicting a 50 μs delay. X-ray bunches forming the 44 μs pulse (light yellow) are shown in gold. (**B**) 3D model of the spectrometer in which the yellow circle represents the sample. Multiple crystals increase the solid angle and are positioned for optimal use of the detector, while a series of slits limit stray scatter/fluorescence. The diagram depicts dispersive reflection onto the detector face due to the Bragg diffraction. (**C**) Sample delivery and positioning system. *Left* Sample-coated thread (red) passes through two narrow guiding needles embedded in plastic goalposts (green) mounted at 45° to the incident beam. A step motor rotates a collection spool in defined intervals to translate the sample through the interaction region between the goalposts. A kinematic mount allows for reproducible sample exchange. *Right* The sample delivery setup, including a timing photodiode (gold) and alignment phosphor, can be exchanged with the goalposts at the exact sample position.
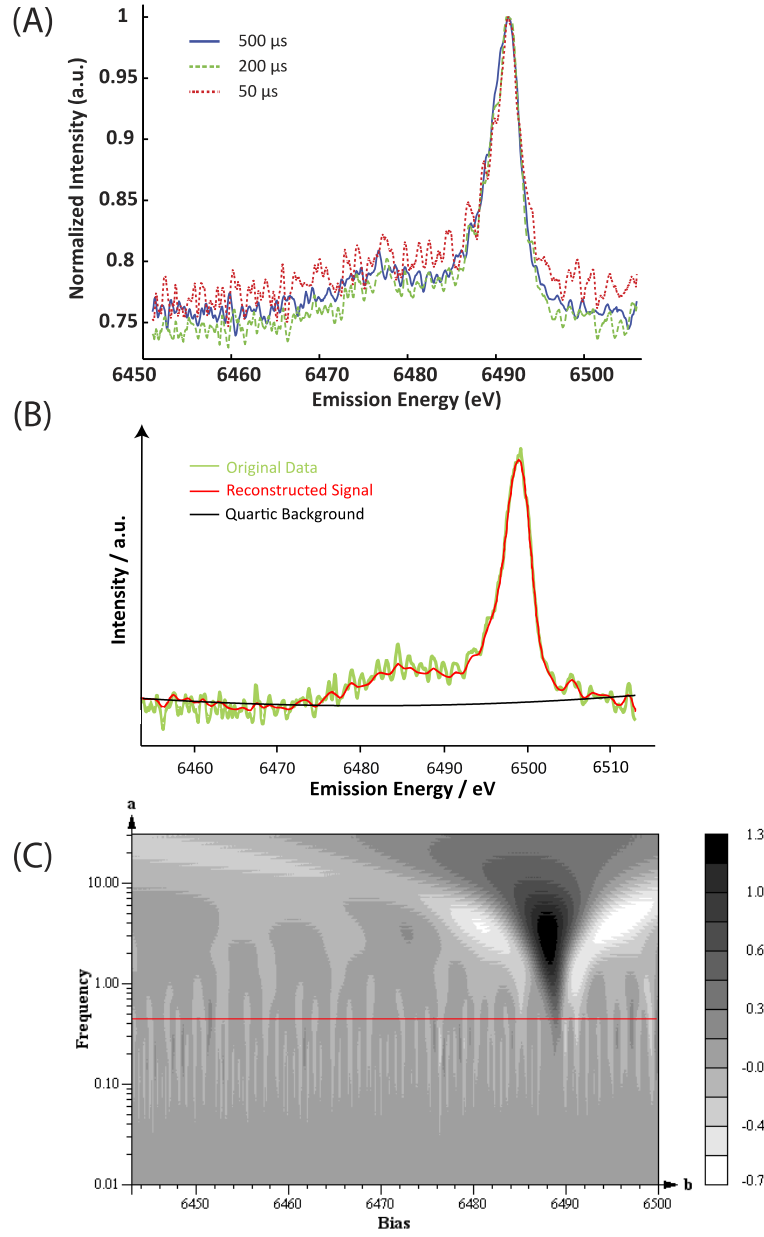
Figure S2. (A) S/N improves with the merging of several data sets aligned with a MnCl$_2$ standard. The 500 µs spectrum is a sum of data sets 1 – 3; the 200 µs spectrum includes data from data sets 2 and 3; and the 50 µs data set is from data set 3 only. See Tables S1 & S7 for details. While background levels from stray scatter entering the detector are significant, making up approximately three quarters of the total signal, the signal to background remains essentially static with little beamtime-to-beamtime variation. **(B)** Example of unprocessed 3F$_{500µs}$ data from data set 2 overlaid with its wavelet-reconstructed spectrum. The quartic background (black line) shown was calculated for the reconstructed signal. **(C)** Example spectrogram for the 500 µs raw data from data set 2. The red line is our chosen frequency cutoff, below which we begin to lose spectral features or experience spectral broadening due to the wavelet reconstruction. The grey-scale color is based on the $w(a, E)$ value at each point.
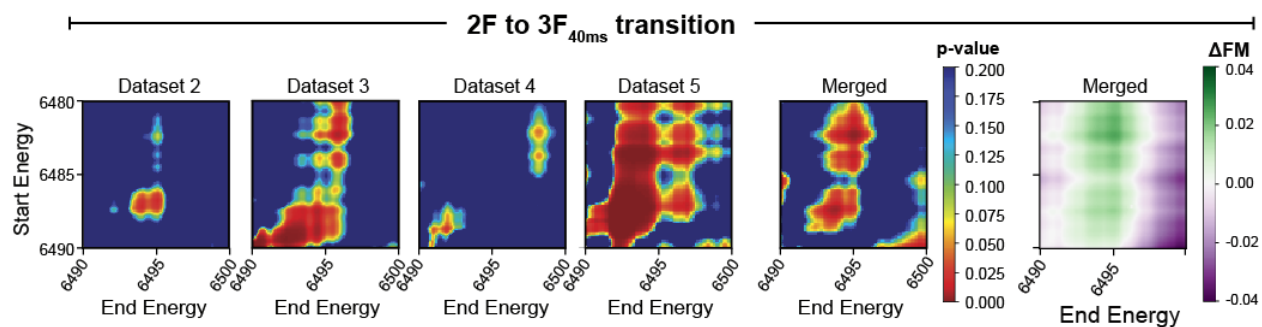
11

Figure S3. Spectral shifts occurring as a result of the 2F→3F transition measured at 40 ms, representative of the majority S_0 state, are characterized using 2-D heatmaps, which graphically illustrate the determined p-values for changes to first moments calculated over the ranges defined by the x and y axes. Strong contours appear in most datasets, indicative of a potentially significant shift. Indeed Table 3, shows p-values of 0.06, very close to our 5% cutoff. The directionality and magnitude of spectral shifts occurring with this S-state transitions are also shown.
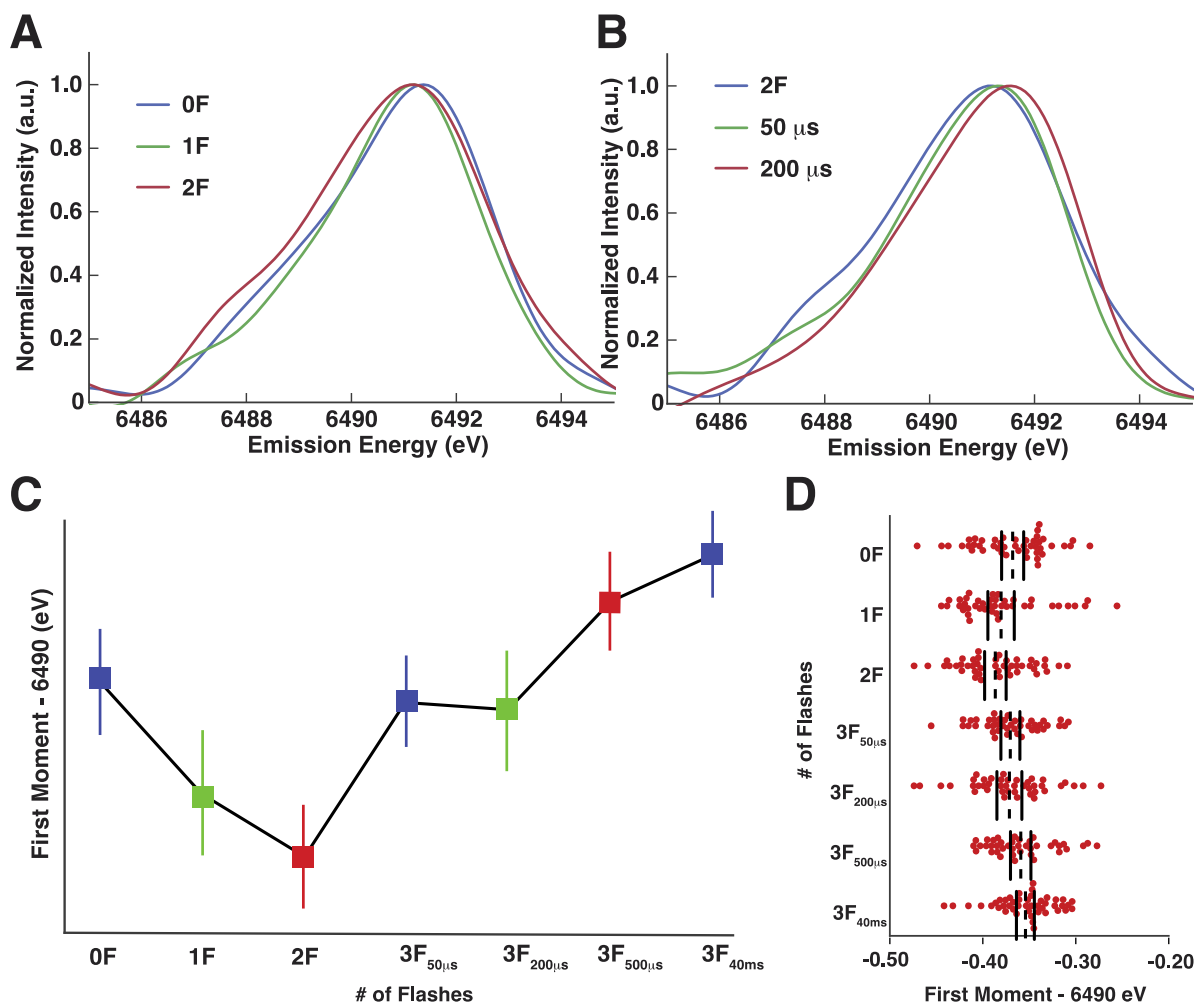
Figure S4. Analysis of an independent fifth dataset confirms results. Note that this dataset was recorded after upgrades at the BioCARS beamline which introduce background that prevent merging this dataset with those presented in the main text. **(A)** and **(B)** Fully processed (wavelet smoothed and background corrected) data which exhibit shifts consistent with other datasets. **(C)** Trends in average first moment from unprocessed spectra. **(D)** A dotplot of first moments calculated for raw data from individual threads with first moments taken over the range 6486.5 – 6492.5 eV. See Figures 2 and 3 for 2-D heatmaps.

Table S1. S-state dependent scan parameters

State	No. of Laser Pulses	α* (μm)	β** (μs)	γ*** (Hz)	Data Sets
S_0	3	600 / 450	40,000	10	1 – 4
S_1	0	300 / 300	n/a	20	1 – 3
S_2	1	600 / 450	500	20	1 – 3
S_3	2	/ 450	500	20	2 – 5
S_{4a}	3	/450	50	20	3 - 5
S_{4b}	3	/ 450	200	20	2 – 5
S_4'	3	600 / 450	500	20	1 – 3,5

* Translation in μm (spool radius: 11.2 / 9.55 mm, for data sets 1 / 2,3,4,5)
** Delay Time
*** Laser and x-ray Frequency

Table S2.   The number of "samples" (i.e. threads) collected per state, per beamtime.

Dataset	# 1	# 2	# 3		# 4	# 5
0F	26	26	26		-	46
1F	26	26	29		-	41
2F	-	26	28	9	33	44
3F (50 μs)	-	-	30	10	35	42
3F (200 μs)	-	26	28	9	35	42
3F (500 μs)	27	26	29		-	40
3F (40 ms)	27	26	29		35	45